Applied Catalysis B: Environmental 307 (2022) 121145

Contents lists available at ScienceDirect

Applied Catalysis B: Environmental

journal homepage: www.elsevier.com/locate/apcatb

Highly dispersed Bi clusters for efficient rechargeable Zn−CO_2 batteries

Miaosen Yang [a,b], Shuai Liu [c], Jiaqiang Sun [d], Mengmeng Jin [c], Rao Fu [a,*], Shusheng Zhang [e], Hongyi Li [f,*], Zhiyong Sun [g], Jun Luo [c], Xijun Liu [h,*]

[a] School of Chemical Engineering, Northeast Electric Power University, Jilin 132012, China
[b] Nanchang Institute of Technology, Nanchang 330044, China
[c] Institute for New Energy Materials and Low-Carbon Technologies, Tianjin Key Lab for Photoelectric Materials & Devices, School of Materials Science and Engineering, Tianjin University of Technology, Tianjin 300384, China
[d] State Key Laboratory of Coal Conversion, Institute of Coal Chemistry, Chinese Academy of Sciences, Taiyuan 030001, Shanxi, China
[e] College of Chemistry, Zhengzhou University, Zhengzhou 450000, China
[f] Guangzhou Panyu Polytechnic, Guangzhou 511483, China
[g] State Key Laboratory for Marine Corrosion and Protection, Luoyang Ship Material Research Institute (LSMRI), Qingdao 266273, China
[h] MOE Key Laboratory of New Processing Technology for Non-Ferrous Metals and Materials, and Guangxi Key Laboratory of Processing for Non-Ferrous Metals and Featured Materials, School of Resource, Environments and Materials, Guangxi University, Nanning 530004, China

ARTICLE INFO

Keywords:
Carbon dioxide electrolysis
Zn−CO_2 battery
Bi clusters
Carbon neutral
Hollow carbon spheres

ABSTRACT

Zn−CO_2 batteries hold great promise for carbon-neutral and electricity generation simultaneously, whereas the main obstacle is the development of electrocatalysts with high activity and durability towards CO_2 reduction reaction (CRR). Herein, we design atomically dispersed Bi clusters supported on hollow carbon spheres (BiC/HCS) for effectively reducing CO_2 to formate, which shows the highest faradaic efficiency of 97 ± 2% at − 0.6 V vs RHE, being comparable to the previously best reported values of Bi-based materials. Experimental and theoretical analyses reveal that the atomic-level Bi_x clusters not only enable high CO_2 adsorption but also stabilize the key *HCOO intermediate with a low free energy barrier. Further, an assembled rechargeable Zn−CO_2 battery with BiC/HCS as the cathode achieves a peak power density of 7.2 ± 0.5 mW cm^{-2} as well as an impressive rechargeability of 200 cycles. This work provides a promising alternative for CO_2 utilization and energy storage by Zn−CO_2 batteries.

Graphical Abstract

Bi clusters anchored on hollow carbon spheres have developed as an excellent cathode for Zn−CO_2 battery. The catalyst presents a maximal formate faradaic efficiency of 97 ± 2% at − 0.6 V vs RHE as well as good durability. The assembled Zn−CO_2 battery achieves a peak power density of 7.2 ± 0.5 mW cm^{-2} and energy efficiency of 68.9% (@ 3 mA cm^{-2}), and a more than 200 cycle rechargeability.

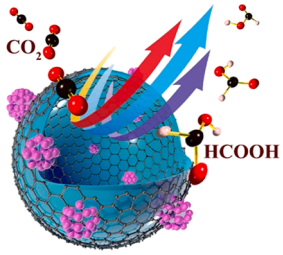

* Corresponding authors.
E-mail addresses: 20132482@neepu.edu.cn (R. Fu), 422340661@qq.com (H. Li), liuxjtjut@163.com (X. Liu).

https://doi.org/10.1016/j.apcatb.2022.121145
Received 12 August 2021; Received in revised form 25 December 2021; Accepted 23 January 2022
Available online 26 January 2022

1. Introduction

The excessive anthropogenic CO_2 emissions induce serious energy crisis and global warming issues, and therefore many efforts have been devoted to realizing the carbon neutral [1–4]. In this regard, electrocatalytic CO_2 reduction reaction (CRR) is a appealing solution due to its versatility, energy efficiency, and cost effectiveness [5–20]. However, the reported CRR progresses were typically achieved in an H-cell or membrane electrode assembly system that require massive energy inputs. There, accordingly, have been recent studies on the developing metal−CO_2 batteries that combine CO_2 fixation and electricity generation simultaneously [21–24]. This newly energy storage system may be also potentially applied in the Mars exploration.

Nevertheless, despite achieving great advancements, these metal−CO_2 batteries (for example Li−CO_2 [ref.25] and Na−CO_2 [refs.26,27] batteries) still suffer from poor selectivity and limited cycling performance. It has a correspondingly great potential for developing aqueous Zn−CO_2 batteries [21,23,28,29], constructing with inert Zn and aqueous catholytes, which enable producing valuable chemicals accompanied by electricity output. Unlike Li/Na−CO_2 batteries, aqueous Zn−CO_2 batteries can be capable of catalyzing the conversion of CO_2 to value-added chemicals, such as CO, hydrocarbons and acids [21]. Additionally, such batteries can alleviate the accumulation of solid products [22]. To realize rechargeable Zn−CO_2 batteries, bifunctional cathodes toward CRR and O_2 evolution reaction (OER) are highly desired. Thus far, a few bifunctional electrocatalysts have been designed for Zn−CO_2 batteries, including noble metals, metal phosphides, and carbon-based materials [22,29–32]. Among them, atomic-level catalysts [29–31,33–35], particularly for single-atom (SA) catalysts, have been confirmed to possess enhanced CRR activity and tunable selectivity due to their high atom utilization efficiency, unique electronic structure, and unsaturated chemical environment. For instance, Zheng et al. reported a reversible aqueous Zn−CO_2 battery based on the CO_2-to-CO conversion by Cu SAs with a peak power density of 0.6 mW cm^{-2} [30]. Wang et al. also prepared a rechargeable Zn–CO_2 battery with Fe SAs as the cathode to achieve a maximal power density of 0.5 mW cm^{-2} [31]. But it should be noted that these batteries with CO as the main CRR product usually exhibited a low power density, making their practical application challenging. Consequently, the optimization of CRR electrocatalysts in Zn−CO_2 battery to generate a large energy density should be highly desirable but is yet still challenging.

Herein, we developed atomically dispersed Bi clusters supported on hollow carbon spheres (namly BiC/HCS) by the pyrolytic treatment of bismuth acetate and carbon precursor. As a result, BiC/HCS presented good performance for CRR toward formate production with a faradaic efficiency (FE) of 97 ± 2% at − 0.6 V versus reversible hydrogen electrode (vs RHE) which is comparable with the most existed Bi-based CRR catalysts (see detials in Table S1). Moreover, the designed catalyst showed negligible decay in terms of the FE and current density under 60-h electrolysis. More importantly, the as-constructed rechargeable Zn−CO_2 battery with the cathode of BiC/HCS delivered a peak power density of 7.2 ± 0.5 mW cm^{-2} and a rechargeability up to 200 cycles, and these values are better than the recent reported Zn–CO_2 batteries produced by porous Pd [32], N dopants and oxygen vacancies co-doped SnO_2 nanosheet [14], and Bi nanoparticles [36]. Meanwhile, the prepared battery demonstrated a energy efficiency of approximately 68.9%. for formate production at the charging current density of 3 mA cm^{-2}. The obtained formate target product realized by our designed Zn–CO_2 battery is more desirable as compared to CO due to its wider application in agricultural and industrial production [21]. Combining experiments and theoretical investigations, the atomic-scale Bi clusters not only enable high CO_2 adsorption but also stabilize the key *HCOO moiety with a low free energy barrier, and thereby improving the performance of the rechargeable Zn−CO_2 batteries. The present work offers an attractive strategy for eco-efficient CO_2 utilization by Zn−CO_2 batteries.

2. Experimental section

2.1. Synthesis of BiC/HCS

The synthesis of hollow carbon spheres (HCS) was obtained according to our previous work [37]. Then, 5 mg HCS was added into a 50-mL solution containing 0.5 mg $NaBH_4$ and stirred for 30 min. After that, a 20-mL solution containing 2 mg Bismuth(III) acetate was dropped into the above mixture. After stirring for 2 h, the resultant was separated by centrifugation and washed with ethanol and deionized water. Last, the powder was pyrolyzed under 500 °C at Ar atmosphere for 1 h with a heating rate of 5 °C min^{-1}.

2.2. Synthesis of BiNP/HCS

The synthetic method for BiNP/HCS was the same as that for BiC/HCS except that the Bismuth(III) acetate addition was 100 mg.

2.3. Characterizations

TEM, HAADF-STEM characterizations and EDS elemental mappings were acquired on an FEI Talos F200X S/TEM. XRD patterns were recorded by an X-ray diffractometer (Rigaku SmartLab 9 kW) at a scan rate of 10 min^{-1} with Cu Kα radiation (λ = 0.154598 nm). XPS spectra were collected on a Thermo Scientific K-alpha XPS system (Thermo Fisher Scientific, UK) with the Al Kα radiation as the X-ray source, and the C 1 s peak was referred to the binding energy of 284.8 eV. The XAFS experiment was carried out at Beamline 1W1B at BSRF. Data of XAFS were processed using the Athena and Artemis programs of the IFEFFIT package based on FEFF 6.

2.4. CRR performance

Electrochemical tests were performed with an electrochemical station (CHI 760E) in an H-type reactor with 0.1 M $KHCO_3$ solution. The two compartments were separated by a Nafion membrane. Ag/AgCl and graphite rod were used as the reference and counter electrodes, respectively. Carbon paper (HESEN, HCP120, 1 cm^2) coated with the catalyst was used as the working electrode. The catalyst loading was 1 mg cm^{-2}. Prior to the CRR, the cathodic electrolyte was saturated with CO_2/Ar for 30 min, and the rate of CO_2 flow was 20 mL min^{-1}. The LSV curves were performed at a sweep rate of 10 mV s^{-1}. *i*R compensation was applied to all initial data. All of the potential values were calculated based on the equation: $E_{RHE} = E_{Ag/AgCl} + 0.0591 \times pH + 0.197$. The gas products were detected by gas chromatography (Agilent GC-7890) equipped with a flame ionization detector (FID) and a thermal conductivity detector (TCD). The liquid products were analyzed by ^{1}H NMR on AVANCE AV III 400.

2.5. Fabrication of Zn−CO_2 batteries

According to our previous work [17], an aqueous rechargeable Zn−CO_2 battery was assembled using BiC/HCS as the cathode, and a 10 cm^2 Zn plate was applied as the anode. 0.8 M $KHCO_3$ was used as catholyte, and 6 M KOH + 0.2 M $Zn(CH_3COO)_2$ was applied as anolyte. The two compartments were separated by a bipolar membrane. The flow rate of CO_2 was kept at 20 sccm during the testing and the CO_2 was always injected into the cathodic electrolyte.

2.6. Theoretical details

All theoretical simulations in this work were conducted on Vienna Ab-initio Simulation Package (VASP) based on the density functional theory (DFT). The projector augmented-wave (PAW) method was employed for describing the ion-electron interactions. The Perdew-Burke-Ernzerhof (PBE) functional was used to analyze the electron-

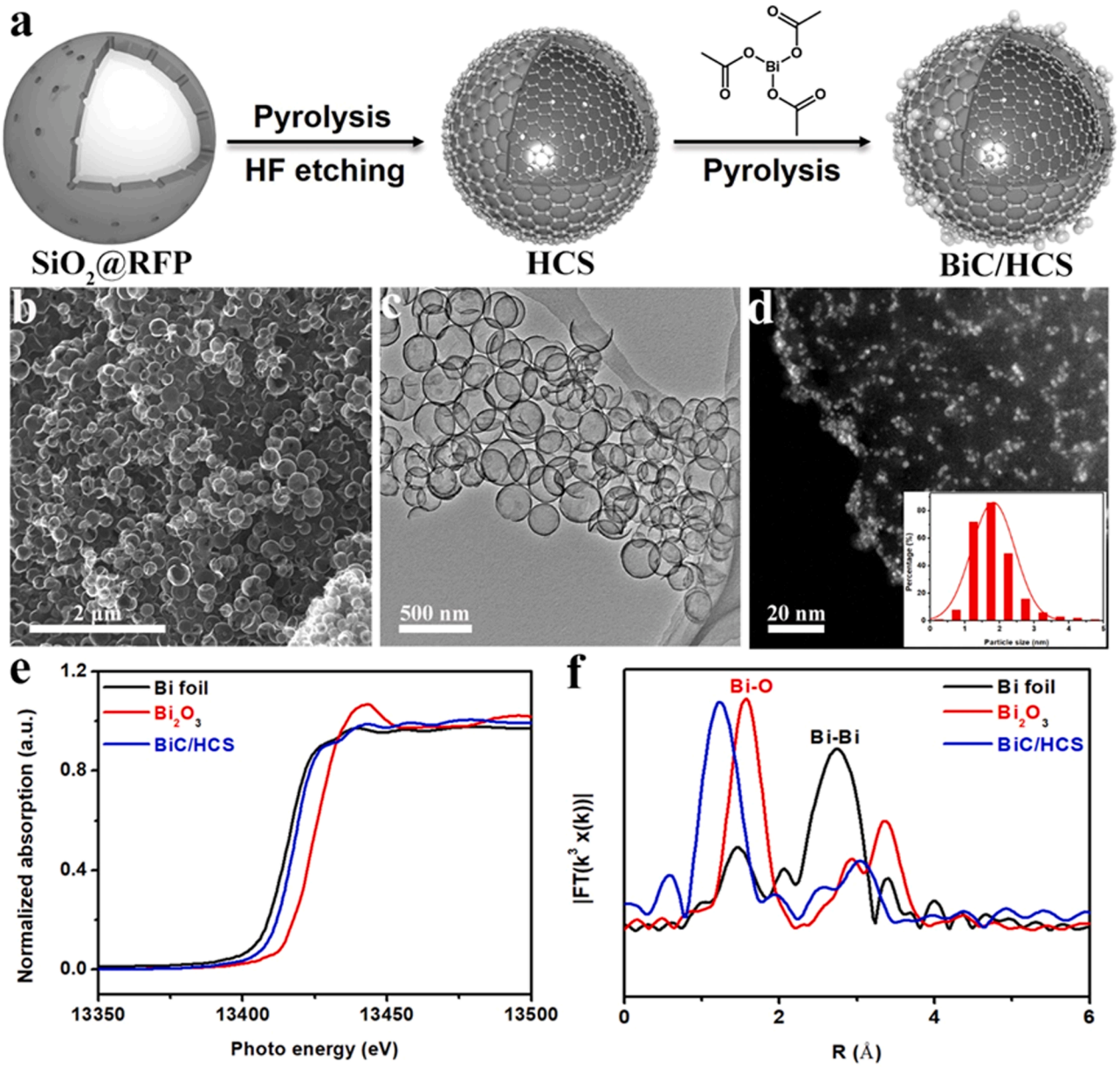

Fig. 1. Synthesis and characterizations of BiC/HCS. a) Schematic illustration of the synthesis procedure. b) SEM image. c) TEM image. d) HAADF-STEM image and the inset of size distribution. e) Normalized XANES spectra at Bi L_3-edge. f) FT-EXAFS spectra.

electron exchange correlations. In all DFT models, the cutoff energy of the plane wave basis sets was set to be 400 eV. The residual force for optimizing atom positions was less than 0.02 eV/Å. The free energy profiles of the CO_2 to formate on BiC/HCS and BiNP/HCS was calculated following Li's study [9].

3. Results and siscussion

3.1. Synthesis and structural characterization

As illustrated in Fig. 1a, BiC/HCS was synthesized by two steps: 1) chemically etching carbon coated on SiO_2 spheres with the aid of HF [37]; and 2) thermal depositing Bi clusters on the above-obtained hollow carbon spheres (see more details in Experimental sections). The unique hollow structural feature can provide a large surface area to support a high loading of active sites [38–41]. Field emission scanning electron microscopy (FESEM) image in Fig. 1b clearly demonstrated the hollow structure feature of BiC/HCS. The average size of the prepared carbon spheres was estimated to be ~500 nm as revealed by the transmission electron microscopy (TEM) image (Fig. 1c). It should be noted that there no Bi crystalline compounds were observed, which is consistent with X-ray diffraction (XRD) pattern and atomic-resolution high-angle annular dark-field scanning TEM (HAADF-STEM) image (Figs. S1 and S2). Magnified HAADF-STEM image and elemental mapping (Fig. 1d and S3) showed the presence of abundant atomically dispersed Bi-related clusters. The size of these clusters was measured to be 1.79 nm. Bi nanoparticles anchored on HCS (denoted as BiNP/HCS) were also prepared as comparison (Figs. S4 and S5).

Fig. 1e depicted the normalized X-ray absorption near edge spectroscopy (XANES) of BiC/HCS and the references (Bi foil and Bi_2O_3 powder). Clearly, the absorption edge of BiC/HCS is located between those of Bi foil and Bi_2O_3, indicative of the average valence of Bi species in BiC/HCS being situated between Bi^0 and Bi^{3+} [42,43]. This is in line with the high resolution Bi 4 f X-ray photoelectron spectroscopy (XPS) spectrum (Fig. S6). Fig. 1f displayed the Fourier transform (FT) k^3-weighted $\chi(k)$ functions of the extended X-ray absorption fine

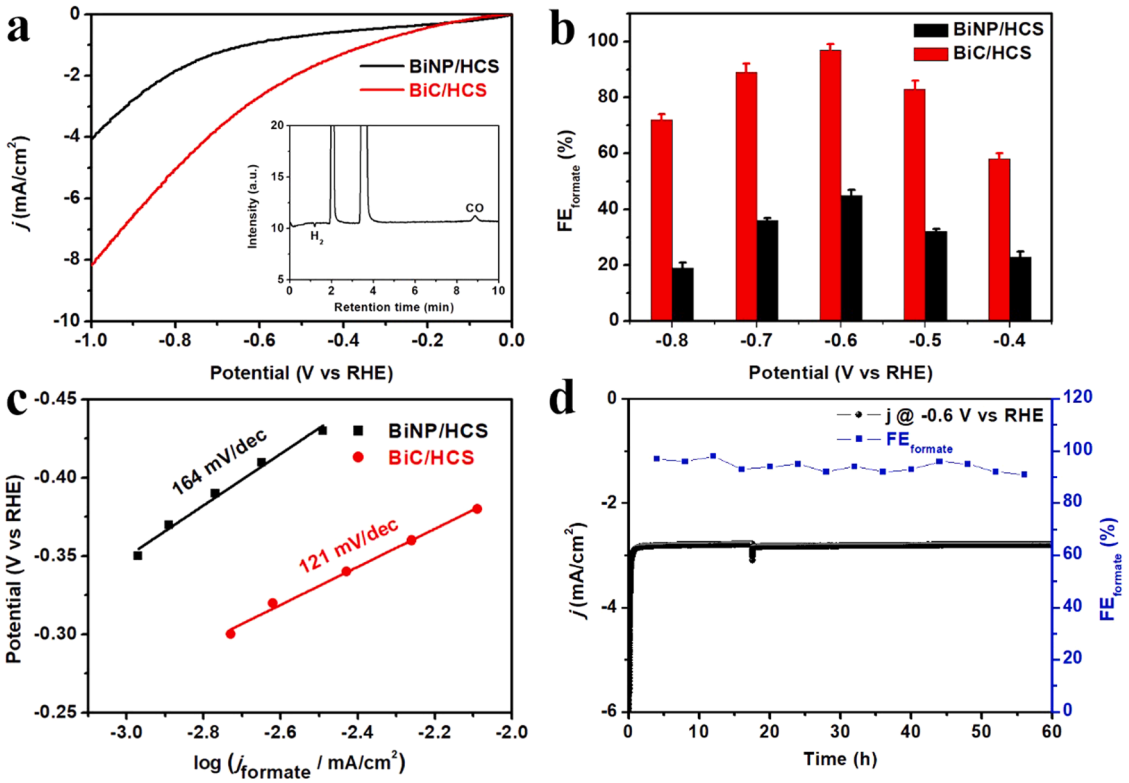

Fig. 2. CRR performance of BiC/HCS. a) CRR LSV curves in CO_2-saturated 0.1 M $KHCO_3$. The inset is the GC spectrum recorded at − 0.6 V vs RHE under CO_2 electrolysis. b) $FE_{formate}$ values at different applied potentials. Note that the error bars here are obtained according to three independent test results. c) CRR Tafel plots. d) The $FE_{formate}$ and current density of BiC/HCS recorded in 60-h stability test at − 0.6 V vs RHE.

structure (EXAFS) spectrum of BiC/HCS, yielding a dominant peak corresponding to Bi–C coordination at ~1.5 Å [42]. These above observations confirmed the formation of highly dispersed Bi_x clusters on hollow carbon spheres. In addition, the content of Bi was detected to be 5.6 wt% by inductively coupled plasma atomic emission spectroscopy (ICP-AES).

3.2. CCR performance

The CRR electrocatalytic activities of BiC/HCS and BiNP/HCS were further evaluated in a typical H-cell with CO_2-saturated 0.1 M $KHCO_3$ under ambient conditions [44]. Noted that all the reported potential were converted into the RHE using Nernst equation. As shown in Fig. S7, the reduction current density of BiC/HCS recorded in CO_2-saturated electrolyte from the linear sweep voltammetry (LSV) measurements was obviously higher than that in Ar-saturated ones, indicating that BiC/HCS was active for CO_2 electroreduction. Meanwhile, the current density for CRR on BiC/HCS was much higher than that on BiNP/HCS (Fig. 2a). For example, BiC/HCS exhibited a 5.09 mA cm^{-2} at − 0.8 V vs RHE, which is 2.80 times higher than that of BiNP/HCS. In addition, when adopting a concentrated electrolyte or a carbon paper with a gas diffusion layer, a higher current density could be achieved (Figs. S8 and S9). We noted that the improved CRR activity of BiC/HCS is not merely due to its larger electrochemically active surface area (ECSA), as confirmed by the ECSA-corrected LSV curves in Fig. S10, and further in-depth understanding of the enhanced CRR activity on BiC/HCS will be discussed later.

The chromatography (GC) and nuclear magnetic resonance (NMR) spectrometer were employed to identify CRR products in the 2-h potentiostatic electrolysis. The detected liquid product over BiC/HCS was only formate (Fig. S11), while the gaseous products were H_2 and CO (inset of Fig. 2a). The obtained FE values at different applied potentials were given in Fig. 2b, BiC/HCS achieved a maximal $FE_{formate}$ of 97 ± 2% at − 0.6 V vs RHE, while BiNP/HCS only yielded an optimal $FE_{formate}$ of 45 ± 2% at − 0.8 V vs RHE, which is significantly lower than BiC/HCS. Also, the CRR performance of BiC/HCS is comparable with the best reported results of Bi-based catalysts (Table S1). No formate was observed during the electrolysis performed in Ar-saturated catholyte on BiC/HCS, suggesting that the formate was derived from the CO_2-to-formate conversion (Fig. S12). Besides, the size effect of BiC/HCS on the CRR activity was also examined (Figs. S13 and S14), suggesting that when the average size increased, the maximal $FE_{formate}$ value initially increased, reached the highest point at 1.79 nm and then decreased.

The Tafel slope, as an indicator to describe the CRR kinetics, was presented in Fig. 2c, yielding a value of 121 mV dec^{-1} for BiC/HCS that close to theoretical one [5] (118 mV dec^{-1}), indicating the first single electron transfer to CO_2 molecule is the rate-determining step on BiC/HCS. In addition, the larger Tafel slope achieved by BiNP/HCS, implying a slow CRR kinetics [45]. Further, the CRR stability of BiC/HCS was examined by prolonged chronopotentiometry under the optimal potential. Attractively, BiC/HCS displayed a good durability up to 30 h (Fig. 2d), during which the $FE_{formate}$ maintained over 90% and the current density was stable. The noise in the chronoamperometric response maybe due to the disturbance of the CO_2 flow. In addition, HAADF-STEM characterization further verified the chemical stability of Bi clusters on the hollow carbon spheres (Fig. S15).

Also, it should be mentioned that oxygen evolution reaction (OER) proceeds on BiC/HCS during the discharging process [21,24]. Therefore, the OER activity of BiC/HCS was evaluated in 0.8 M $KHCO_3$ solution. As depicted in Fig. S16a, BiC/HCS required a lower overpotential of 280 mV to reach 10 mA cm^{-2} in comparison with the BiNP/HCS counterpart (310 mV). Besides, the observed smaller Tafel slope of 133 mV dec^{-1} on BiC/HCS compared to BiNP/HCS (Fig. S16b), implying the faster OER kinetics over BiC/HCS [46]. As revealed by the above experimental results, the developed BiC/HCS shows good performance toward CRR and OER simultaneously, making it an appealing catalyst

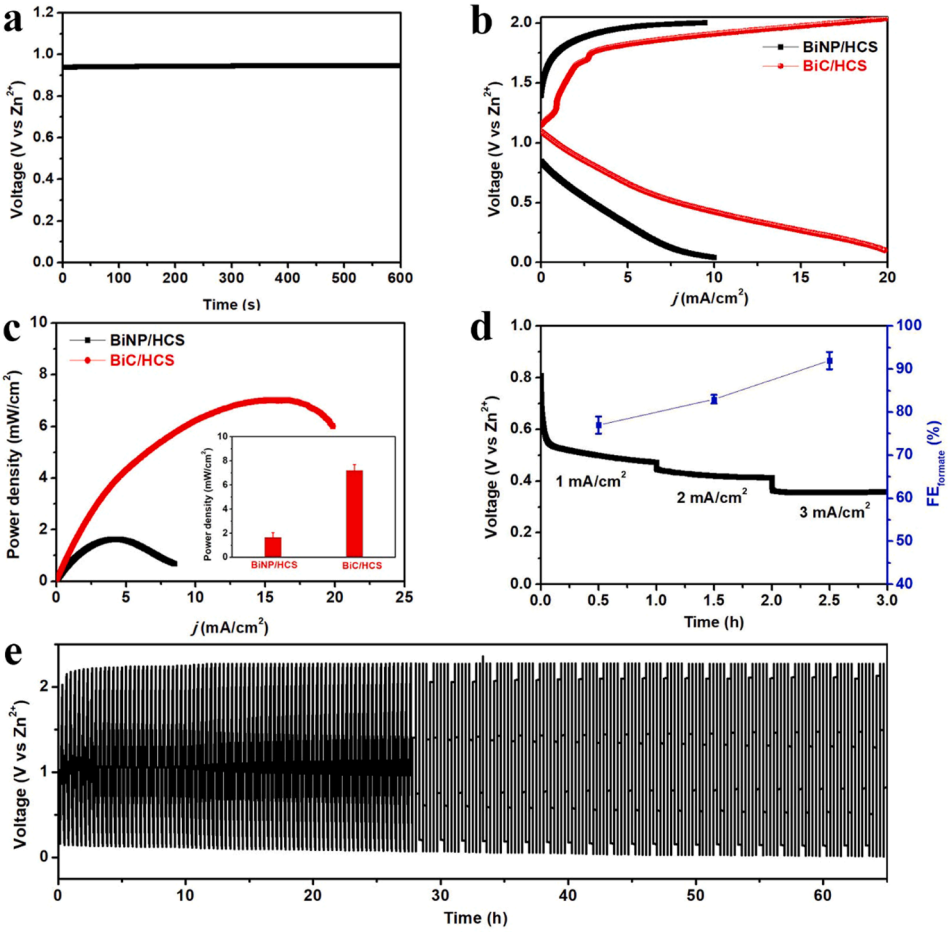

Fig. 3. Performance of the aqueous rechargeable Zn–CO_2 cell based on BiC/HCS. a) Open-circuit plots. b) Discharge and charge polarization curves with a scanning rate of 10 mV s^{-1}. c) Power density curves. Inset is the peak power density of BiC/HCS and BiNP/HCS. d) Galvanostatic discharge curves at different current densities and the corresponding $FE_{formate}$ values. e) Galvanostatic discharge–charge cycling curves at 1.0 mA cm^{-2}.

for the aqueous rechargeable Zn–CO_2 batteries.

3.3. Zn-CO_2 battery performance

We further investigate the practical application of BiC/HCS as the cathode in an aqueous Zn–CO_2 battery. The assembled battery delivered an open circuit voltage of 0.94 V for BiC/HCS (Fig. 3a), which agrees well with the theoretical value (0.96 V) [26]. Fig. 3b showed the discharge and charge polarization curves for Zn–CO_2 batteries based on the BiC/HCS and BiNP/HCS cathodes, respectively. According to previously reported literature [30], the cathodic reaction of CRR took place accompanied by the dissolution of Zn plate to Zn^{2+} at the anode during the discharging; while for the charging, OER occurred on the cathode and Zn^{2+} ions were reduced back to the Zn metal. Strikingly, the Zn–CO_2 battery with the cathode of BiC/HCS achieved a maximal power density of 7.2 ± 0.5 mW cm^{-2} at 19.4 mA cm^{-2} (Fig. 3c), which is comparable to those of the best-reported values (see details in Table S2). Additionally, a peak power density of 1.6 ± 0.4 mW cm^{-2} reached on BiNP/HCS, significantly lower than that on BiC/HCS.

Furthermore, at a discharge current density of 1, 2 and 3 mA cm^{-2}, BiC/HCS exhibited $FE_{formate}$ values of 77 ± 2, 83 ± 1, and 92 ± 2%, respectively (Fig. 3d). This indicates its high selectivity of the CO_2-to-formate conversion. This change in the selectivity of CO_2 reduction strongly depends on the deviations to the equilibrium potential for formate production and the competitive hydrogen evolution at different applied cell voltages [47,48]. The corresponding energy efficiencies were calculated to be approximately 51.2%, 62.7%, and 68.9%, respectively. When the BiC/HCS based Zn-CO_2 battery was recycled at 1 mA cm^{-2} (Fig. 3e), it maintained good rechargeability over 200 cycles (up to 65 h). Of note, the Zn-CO_2 battery with BiC/HCS cathode is more cost-effective than the recently reported Zn-CO_2 batteries produced by the noble metals such as Ir@Au and Pd catalysts [22,32].

3.4. DFT calculations

To uncover the nature of superior CRR reactivity of BiC/HCS, density functional theory (DFT) calculations were performed [9]. According to the EXAFS spectra, a model of rhombic Bi_4 clusters anchored on carbon support was taken into consideration for BiC/HCS. For comparison, the DFT model for Bi (012) for BiNP/HCS was built up (Fig. S17). It has been documented that the initial CO_2 molecule adsorption is the prerequisite for the following proton–electron transfer [49–53], and therefore the CO_2 adsorption isotherms were added (Fig. 4a).

As seen, the presence of atomically dispersed Bi_4 clusters on the hollow carbon spheres can provide more active sites to adsorb higher amounts of CO_2 [54]. Of note, the previous studies confirmed the formation of *HCOO intermediates was the potential limiting step [5,55], which is the initial reduction barrier for the CO_2-to-formate conversion. As revealed by Fig. 4b, BiC/HCS could stabilize the *HCOO intermediate on catalyst surface, which favors the CRR. Moreover, the free energy profiles demonstrated that there is a reduced free energy barrier (1.04 eV → 0.79 eV) for the formation of *HCOO on BiC/HCS under an applied potential (Fig. 4c). Interestingly, Bi (012) also favor the formation of *HCOO with a comparable energy barrier (0.96 eV) in

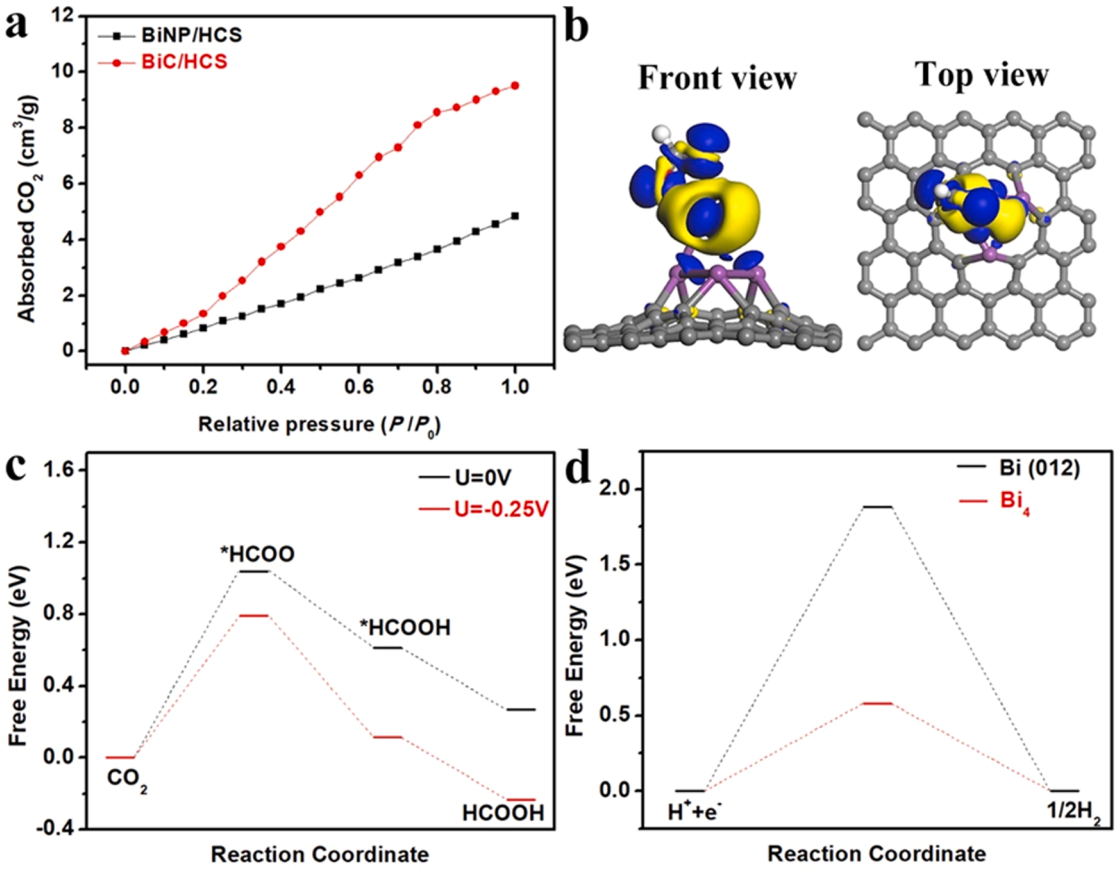

Fig. 4. Mechanistic insights for the CRR improvement of BiC/HCS. a) CO_2 adsorption isotherms. b) Charge density difference of the *HCOO-adsorbed configuration. c) Free-energy diagrams for HCOOH formation. d) HER free-energy diagrams.

comparison with BiNP/HCS (Fig. S18), which is consistent with the literature [56]. Further, the competitive hydrogen evolution reaction (HER) energy barriers on both BiC/HCS and BiNP/HCS were also calculated and the results were shown in Fig. 4d, from which it can be concluded that the HER process was well suppressed on BiC/HCS [57–59]. These DFT results are in line with the electrocatalytic performance (Fig. 2). Consequently, the CRR on BiC/HCS was more energetic-favorable than that on BiNP/HCS.

4. Conclusion

In summary, we here designed an efficient and stable catalyst composed of atomically dispersed Bi clusters anchored on hollow carbon spheres as the cathode for Zn−CO_2 battery. BiC/HCS delivered a high selectivity and durability for the CO_2-to-formate conversion with a maximal $FE_{formate}$ of 97 ± 2% at − 0.6 V vs RHE as well as kept stable up to 60 h. Further, the Zn−CO_2 battery based on the BiC/HCS cathode presented an open-circuit potential of 0.94 V, a peak power density of 7.2 ± 0.5 mW cm^{-2}, and good rechargeability (up to 200 cycles). In addition, this battery also showed a high $FE_{formate}$ of 92 ± 2% and an energy efficiency of approximately 68.9% at a discharge current density of 3 mA cm^{-2}. Our work offers an opportunity for realizing high-efficency CO_2 fixation and energy storage at the same time by using Zn−CO_2 batteries with metal oxide clusters as the cathode.

CRediT authorship contribution statement

Miaosen Yang: Data curation, Methodology, Investigation. **Shuai Liu:** Methodology. **Jiaqiang Sun:** Methodology. **Mengmeng Jin:** Data curation, Methodology. **Rao Fu:** Supervision, Writing – review & editing. **Shusheng Zhang:** Methodology. **Hongyi Li**: Supervision, Writing – review & editing. **Zhiyong Sun:** Writing – review & editing. **Jun Luo:** Project administration. **Xijun Liu**: Conceptualization, Project administration, Supervision.

Declaration of Competing Interest

The authors declare that they have no known competing financial interests or personal relationships that could have appeared to influence the work reported in this paper.

Acknowledgments

This work was financially supported by National Natural Science Foundation of China (22075211, 21601136, 51971157, and 51621003), and Guangzhou Panyu Polytechnic Science & Technology Project No. 2021KJ01. The authors acknowledge Beijing PARATERA Tech CO., Ltd. for providing HPC resources that have contributed to the research results reported within this paper.

Appendix A. Supporting information

Supplementary data associated with this article can be found in the online version at doi:10.1016/j.apcatb.2022.121145.

References

[1] S.S. Myers, A. Zanobetti, I. Kloog, P. Huybers, A.D.B. Leakey, A.J. Bloom, E. Carlisle, L.H. Dietterich, G. Fitzgerald, T. Hasegawa, N.M. Holbrook, R.L. Nelson, M.J. Ottman, V. Raboy, H. Sakai, K.A. Sartor, J. Schwartz, S. Seneweera, M. Tausz, Y. Usui, Increasing CO_2 threatens human nutrition, Nature 510 (2014) 139–142, https://doi.org/10.1038/nature13179.

[2] H. Bao, Y. Qiu, X. Peng, J.-a Wang, Y. Mi, S. Zhao, X. Liu, Y. Liu, R. Cao, L. Zhuo, J. Ren, J. Sun, J. Luo, X. Sun, Isolated copper single sites for high-performance electroreduction of carbon monoxide to multicarbon products, Nat. Commun. 12 (2021) 238, https://doi.org/10.1038/s41467-020-20336-4.

[3] Y. Mi, Y. Qiu, Y. Liu, X. Peng, M. Hu, S. Zhao, H. Cao, L. Zhuo, H. Li, J. Ren, X. Liu, J. Luo, Cobalt−iron oxide nanosheets for high-efficiency solar-driven CO_2−H_2O coupling electrocatalytic reactions, Adv. Funct. Mater. 30 (2020), 2003438, https://doi.org/10.1002/adfm.202003438.

[4] F. Lv, N. Han, Y. Qiu, X. Liu, J. Luo, Y. Li, Transition metal macrocycles for heterogeneous electrochemical CO_2 reduction, Coord. Chem. Rev. 422 (2020), 213435, https://doi.org/10.1016/j.ccr.2020.213435.

[5] F. Lü, H. Bao, Y. Mi, Y. Liu, J. Sun, X. Peng, Y. Qiu, L. Zhuo, X. Liu, J. Luo, Electrochemical CO_2 reduction: from nanoclusters to single atom catalysts, Sustain. Energy Fuels 4 (2020) 1012–1028, https://doi.org/10.1039/C9SE00776H.

[6] N. Han, M. Sun, Y. Zhou, J. Xu, C. Cheng, R. Zhou, L. Zhang, J. Luo, B. Huang, Y. Li, Alloyed palladium–silver nanowires enabling ultrastable carbon dioxide reduction to formate, Adv. Mater. 33 (2021), 2005821, https://doi.org/10.1002/adma.202005821.

[7] L. Han, X. Liu, J. He, Z. Liang, H.-T. Wang, S.-M. Bak, J. Zhang, A. Hunt, I. Waluyo, W.-F. Pong, J. Luo, Y. Ding, R.R. Adzic, H.L. Xin, Modification of the coordination environment of active sites on MoC for high-efficiency CH_4 production, Adv. Energy Mater. 11 (2021), 2100044, https://doi.org/10.1002/aenm.202100044.

[8] A. Vasileff, C. Xu, Y. Jiao, Y. Zheng, S.-Z. Qiao, Surface and interface engineering in copper-based bimetallic materials for selective CO_2 electroreduction, Chem 4 (2018) 1809–1831, https://doi.org/10.1016/j.chempr.2018.05.001.

[9] N. Han, Y. Wang, H. Yang, J. Deng, J. Wu, Y. Li, Y. Li, Ultrathin bismuth nanosheets from in situ topotactic transformation for selective electrocatalytic CO_2 reduction to formate, Nat. Commun. 9 (2018) 1320, https://doi.org/10.1038/s41467-018-03712-z.

[10] Z. Li, Q. Zeng, Z. Ye, W. Zheng, X. Sang, C.-L. Dong, B. Yang, S. Pardiwala, J. Lu, L. Lei, G. Wu, Y. Hou, An integrated bioelectrochemical system coupled CO_2 electroreduction device based on atomically dispersed iron electrocatalysts, Nano Energy 87 (2021), 106187, https://doi.org/10.1016/j.nanoen.2021.106187.

[11] X. Wang, X. Sang, C.-L. Dong, S. Yao, L. Shuai, J. Lu, B. Yang, Z. Li, L. Lei, M. Qiu, L. Dai, Y. Hou, Proton capture strategy for enhancing electrochemical CO_2 reduction on atomically dispersed metal–nitrogen active sites, Angew. Chem. Int. Ed. 60 (2021) 11959–11965, https://doi.org/10.1002/anie.202100011.

[12] G. Wang, J. Chen, Y. Ding, P. Cai, L. Yi, Y. Li, C. Tu, Y. Hou, Z. Wen, L. Dai, Electrocatalysis for CO_2 conversion: from fundamentals to value-added products, Chem. Soc. Rev. 50 (2021) 4993–5061, https://doi.org/10.1039/D0CS00071J.

[13] X. Wang, Y. Wang, X. Sang, W. Zheng, S. Zhang, L. Shuai, B. Yang, Z. Li, J. Chen, L. Lei, N.M. Adli, M.K.H. Leung, M. Qiu, G. Wu, Y. Hou, Dynamic activation of adsorbed intermediates via axial traction for the promoted electrochemical CO_2 reduction, Angew. Chem. Int. Ed. 60 (2021) 4192–4198, https://doi.org/10.1002/anie.202013427.

[14] Z. Li, A. Cao, Q. Zheng, Y. Fu, T. Wang, K.T. Arul, J.-L. Chen, B. Yang, N.M. Adli, L. Lei, C.-L. Dong, J. Xiao, G. Wu, Y. Hou, Elucidation of the synergistic effect of dopants and vacancies on promoted selectivity for CO_2 electroreduction to formate, Adv. Mater. 33 (2021), 2005113, https://doi.org/10.1002/adma.202005113.

[15] M.T. Tang, H. Peng, P.S. Lamoureux, M. Bajdich, F. Abild-Pedersen, From electricity to fuels: descriptors for C1 selectivity in electrochemical CO_2 reduction, Appl. Catal. B Environ. 279 (2020), 119384, https://doi.org/10.1016/j.apcatb.2020.119384.

[16] L. Wang, P. Liu, Y. Xu, Y. Zhao, N. Xue, X. Guo, L. Peng, Y. Zhu, M. Ding, Q. Wang, W. Ding, Enhanced catalytic activity and stability of bismuth nanosheets decorated by 3-Aminopropyltriethoxysilane for efficient electrochemical reduction of CO_2, Appl. Catal. B Environ. 298 (2021), 120602, https://doi.org/10.1016/j.apcatb.2021.120602.

[17] I. Merino-Garcia, L. Tinat, J. Albo, M. Alvarez-Guerra, A. Irabien, O. Durupthy, V. Vivier, C.M. Sánchez-Sánchez, Continuous electroconversion of CO_2 into formate using 2 nm tin oxide nanoparticles, Appl. Catal. B: Environ. 297 (2021), 120447, https://doi.org/10.1016/j.apcatb.2021.120447.

[18] J. Li, J. Li, X. Liu, J. Chen, P. Tian, S. Dai, M. Zhu, Y.-F. Han, Probing the role of surface hydroxyls for Bi, Sn and In catalysts during CO_2 reduction, Appl. Catal. B Environ. 298 (2021), 120581, https://doi.org/10.1016/j.apcatb.2021.120581.

[19] Z. Yang, H. Wang, X. Fei, W. Wang, Y. Zhao, X. Wang, X. Tan, Q. Zhao, H. Wang, J. Zhu, L. Zhou, H. Ning, M. Wu, MOF derived bimetallic CuBi catalysts with ultra-wide potential window for high-efficient electrochemical reduction of CO_2 to formate, Appl. Catal. B: Environ. 298 (2021), 120571, https://doi.org/10.1016/j.apcatb.2021.120571.

[20] M.J. Kang, C.W. Kim, H.G. Cha, A.U. Pawar, Y.S. Kang, Selective liquid chemicals on CO_2 reduction by energy level tuned rGO/TiO_2 dark cathode with $BiVO_4$ photoanode, Appl. Catal. B Environ. 295 (2021), 120267, https://doi.org/10.1016/j.apcatb.2021.120267.

[21] J. Xie, Y. Wang, Recent development of CO_2 electrochemistry from Li–CO_2 batteries to Zn–CO_2 batteries, Acc. Chem. Res. 52 (2019) 1721–1729, https://doi.org/10.1021/acs.accounts.9b00179.

[22] X. Wang, J. Xie, M.A. Ghausi, J. Lv, Y. Huang, M. Wu, Y. Wang, J. Yao, Rechargeable Zn–CO_2 electrochemical cells mimicking two-step photosynthesis, Adv. Mater. 31 (2019), 1807807, https://doi.org/10.1002/adma.201807807.

[23] S. Gao, Y. Liu, Z. Xie, Y. Qiu, L. Zhuo, Y. Qin, J. Ren, S. Zhang, G. Hu, J. Luo, X. Liu, Metal-free bifunctional ordered mesoporous carbon for reversible Zn-CO_2 batteries, Small Methods 5 (2021), 2001039, https://doi.org/10.1002/smtd.202001039.

[24] Z. Xie, X. Zhang, Z. Zhang, Z. Zhou, Metal–CO_2 batteries on the road: CO_2 from contamination gas to energy source, Adv. Mater. 29 (2017), 1605891, https://doi.org/10.1002/adma.201605891.

[25] Y. Qiao, J. Yi, S. Wu, Y. Liu, S. Yang, P. He, H. Zhou, Li-CO_2 electrochemistry: a new strategy for CO_2 fixation and energy storage, Joule 1 (2017) 359–370, https://doi.org/10.1016/j.joule.2017.07.001.

[26] X. Hu, J. Sun, Z. Li, Q. Zhao, C. Chen, J. Chen, Rechargeable room-temperature Na–CO_2 batteries, Angew. Chem. Int. Ed. 55 (2016) 6482–6486, https://doi.org/10.1002/anie.201602504.

[27] C. Fang, J. Luo, C. Jin, H. Yuan, O. Sheng, H. Huang, Y. Gan, Y. Xia, C. Liang, J. Zhang, W. Zhang, X. Tao, Enhancing catalyzed decomposition of Na_2CO_3 with Co_2MnO_x nanowire-decorated carbon fibers for advanced Na–CO_2 batteries, ACS Appl. Mater. Interfaces 10 (2018) 17240–17248, https://doi.org/10.1021/acsami.8b04034.

[28] X. Hao, X. An, A.M. Patil, P. Wang, X. Ma, X. Du, X. Hao, A. Abudula, G. Guan, Biomass-derived N-doped carbon for efficient electrocatalytic CO_2 reduction to CO and Zn–CO_2 batteries, ACS Appl. Mater. Interfaces 13 (2021) 3738–3747, https://doi.org/10.1021/acsami.0c13440.

[29] W. Ni, Z. Liu, Y. Zhang, C. Ma, H. Deng, S. Zhang, S. Wang, Electroreduction of carbon dioxide driven by the intrinsic defects in the carbon plane of a single Fe–N_4 site, Adv. Mater. 33 (2021), 2003238, https://doi.org/10.1002/adma.202003238.

[30] W. Zheng, J. Yang, H. Chen, Y. Hou, Q. Wang, M. Gu, F. He, Y. Xia, Z. Xia, Z. Li, B. Yang, L. Lei, C. Yuan, Q. He, M. Qiu, X. Feng, Atomically defined undercoordinated active sites for highly efficient CO_2 electroreduction, Adv. Funct. Mater. 30 (2020), 1907658, https://doi.org/10.1002/adfm.201907658.

[31] T. Wang, X. Sang, W. Zheng, B. Yang, S. Yao, C. Lei, Z. Li, Q. He, J. Lu, L. Lei, L. Dai, Y. Hou, Gas diffusion strategy for inserting atomic iron sites into graphitized carbon supports for unusually high-efficient CO_2 electroreduction and high-performance Zn–CO_2 batteries, Adv. Mater. 32 (2020), 2002430, https://doi.org/10.1002/adma.202002430.

[32] J. Xie, X. Wang, J. Lv, Y. Huang, M. Wu, Y. Wang, J. Yao, Reversible aqueous Zinc–CO_2 batteries based on CO_2–HCOOH interconversion, Angew. Chem. Int. Ed. 57 (2018) 16996–17001, https://doi.org/10.1002/anie.201811853.

[33] A. Han, Z. Zhang, X. Li, D. Wang, Y. Li, Atomic thickness catalysts: synthesis and applications, Small Methods 4 (2020), 2000248, https://doi.org/10.1002/smtd.202000248.

[34] W. Ni, Z. Liu, X. Guo, Y. Zhang, C. Ma, Y. Deng, S. Zhang, Dual single-cobalt atom-based carbon electrocatalysts for efficient CO_2-to-syngas conversion with industrial current densities, Appl. Catal. B Environ. 291 (2021), 120092, https://doi.org/10.1016/j.apcatb.2021.120092.

[35] X. Zhang, C. Liu, Y. Zhao, L. Li, Y. Chen, F. Raziq, L. Qiao, S.-X. Guo, C. Wang, G. G. Wallace, A.M. Bond, J. Zhang, Atomic nickel cluster decorated defect-rich copper for enhanced C_2 product selectivity in electrocatalytic CO_2 reduction, Appl. Catal. B Environ. 291 (2021), 120030, https://doi.org/10.1016/j.apcatb.2021.120030.

[36] Y. Wang, L. Xu, L. Zhan, P. Yang, S. Tang, M. Liu, X. Zhao, Y. Xiong, Z. Chen, Y. Lei, Electron accumulation enables Bi efficient CO_2 reduction for formate production to boost clean Zn-CO_2 batteries, Nano Energy 92 (2022), 106780, https://doi.org/10.1016/j.nanoen.2021.106780.

[37] D. Qi, S. Liu, H. Chen, S. Lai, Y. Qin, Y. Qiu, S. Dai, S. Zhang, J. Luo, X. Liu, Rh nanoparticle functionalized heteroatom-doped hollow carbon spheres for efficient electrocatalytic hydrogen evolution, Mater. Chem. Front. 5 (2021) 3125–3131, https://doi.org/10.1039/D1QM00156F.

[38] C. Dong, Q. Yu, R.-P. Ye, P. Su, J. Liu, G.-H. Wang, Hollow carbon sphere nanoreactors loaded with PdCu nanoparticles: void-confinement effects in liquid-phase hydrogenations, Angew. Chem. Int. Ed. 59 (2020) 18374–18379, https://doi.org/10.1002/anie.202007297.

[39] H. Tian, J. Liang, J. Liu, Nanoengineering carbon spheres as nanoreactors for sustainable energy applications, Adv. Mater. 31 (2019), 1903886, https://doi.org/10.1002/adma.201903886.

[40] H. Tian, H. Tian, S. Wang, S. Chen, F. Zhang, L. Song, H. Liu, J. Liu, G. Wang, High-power lithium–selenium batteries enabled by atomic cobalt electrocatalyst in hollow carbon cathode, Nat. Commun. 11 (2020) 5025, https://doi.org/10.1038/s41467-020-18820-y.

[41] S. Ma, P. Su, W. Huang, S.P. Jiang, S. Bai, J. Liu, Atomic Ni species anchored N-doped carbon hollow spheres as nanoreactors for efficient electrochemical CO_2 reduction, ChemCatChem 11 (2019) 6092–6098, https://doi.org/10.1002/cctc.201901643.

[42] X. Yang, Y. Chen, L. Qin, X. Wu, Y. Wu, T. Yan, Z. Geng, J. Zeng, Boost selectivity of $HCOO^-$ using anchored Bi single atoms towards CO_2 reduction, ChemSusChem 13 (2020) 6307–6311, https://doi.org/10.1002/cssc.202001609.

[43] E. Zhang, T. Wang, K. Yu, J. Liu, W. Chen, A. Li, H. Rong, R. Lin, S. Ji, X. Zheng, Y. Wang, L. Zheng, C. Chen, D. Wang, J. Zhang, Y. Li, Bismuth single atoms resulting from transformation of metal–organic frameworks and their use as electrocatalysts for CO_2 reduction, J. Am. Chem. Soc. 141 (2019) 16569–16573, https://doi.org/10.1021/jacs.9b08259.

[44] J. Xu, S. Lai, D. Qi, M. Hu, X. Peng, Y. Liu, W. Liu, G. Hu, H. Xu, F. Li, C. Li, J. He, L. Zhuo, J. Sun, Y. Qiu, S. Zhang, J. Luo, X. Liu, Atomic Fe-Zn dual-metal sites for high-efficiency pH-universal oxygen reduction catalysis, Nano Res. 14 (2021) 1374–1381, https://doi.org/10.1007/s12274-020-3186-x.

[45] J. Xu, S. Lai, M. Hu, S. Ge, R. Xie, F. Li, D. Hua, H. Xu, H. Zhou, R. Wu, J. Fu, Y. Qiu, J. He, C. Li, H. Liu, Y. Liu, J. Sun, X. Liu, J. Luo, Semimetal 1H-SnS_2 enables high-efficiency electroreduction of CO_2 to CO, Small Methods 4 (2020), 2000567, https://doi.org/10.1002/smtd.202000567.

[46] X. Peng, S. Zhao, Y. Mi, L. Han, X. Liu, D. Qi, J. Sun, Y. Liu, H. Bao, L. Zhuo, H. L. Xin, J. Luo, X. Sun, Trifunctional single-atomic Ru sites enable efficient overall

water splitting and oxygen reduction in acidic media, Small 16 (2020), 2002888, https://doi.org/10.1002/smll.202002888.
[47] X. Liu, H. Yang, J. He, H. Liu, L. Song, L. Li, J. Luo, Highly active, durable ultrathin $MoTe_2$ layers for the electroreduction of CO_2 to CH_4, Small 14 (2018), 1704049, https://doi.org/10.1002/smll.201704049.
[48] A. Vasileff, Y. Zheng, S.Z. Qiao, Carbon solving carbon's problems: recent progress of nanostructured carbon-based catalysts for the electrochemical reduction of CO_2, Adv. Energy Mater. 7 (2017), 1700759, https://doi.org/10.1002/aenm.201700759.
[49] J. He, X. Liu, H. Liu, Z. Zhao, Y. Ding, J. Luo, Highly selective electrocatalytic reduction of CO_2 to formate over Tin(IV) sulfide monolayers, J. Catal. 364 (2018) 125–130, https://doi.org/10.1016/j.jcat.2018.05.005.
[50] D.J. Deka, J. Kim, S. Gunduz, M. Aouine, J.-M.M. Millet, A.C. Co, U.S. Ozkan, Investigation of hetero-phases grown via in-situ exsolution on a Ni-doped (La,Sr) FeO_3 cathode and the resultant activity enhancement in CO_2 reduction, Appl. Catal. B Environ. 286 (2021), 119917, https://doi.org/10.1016/j.apcatb.2021.119917.
[51] M. Zhao, Y. Gu, W. Gao, P. Cui, H. Tang, X. Wei, H. Zhu, G. Li, S. Yan, X. Zhang, Z. Zou, Atom vacancies induced electron-rich surface of ultrathin Bi nanosheet for efficient electrochemical CO_2 reduction, Appl. Catal. B Environ. 266 (2020), 118625, https://doi.org/10.1016/j.apcatb.2020.118625.
[52] F. Li, G.H. Gu, C. Choi, P. Kolla, S. Hong, T.-S. Wu, Y.-L. Soo, J. Masa, S. Mukerjee, Y. Jung, J. Qiu, Z. Sun, Highly stable two-dimensional bismuth metal-organic frameworks for efficient electrochemical reduction of CO_2, Appl. Catal. B Environ. 277 (2020), 119241, https://doi.org/10.1016/j.apcatb.2020.119241.
[53] H. Song, J.T. Song, B. Kim, Y.C. Tan, J. Oh, Activation of C_2H_4 reaction pathways in electrochemical CO_2 reduction under low CO_2 partial pressure, Appl. Catal. B Environ. 272 (2020), 119049, https://doi.org/10.1016/j.apcatb.2020.119049.
[54] S. Gao, X. Jiao, Z. Sun, W. Zhang, Y. Sun, C. Wang, Q. Hu, X. Zu, F. Yang, S. Yang, L. Liang, J. Wu, Y. Xie, Ultrathin Co_3O_4 layers realizing optimized CO_2 electroreduction to formate, Angew. Chem. Int. Ed. 55 (2016) 698–702, https://doi.org/10.1002/anie.201509800.
[55] B. Zhang, J. Zhang, J. Shi, D. Tan, L. Liu, F. Zhang, C. Lu, Z. Su, X. Tan, X. Cheng, B. Han, L. Zheng, J. Zhang, Manganese acting as a high-performance heterogeneous electrocatalyst in carbon dioxide reduction, Nat. Commun. 10 (2019) 2980, https://doi.org/10.1038/s41467-019-10854-1.
[56] W. Ma, J. Bu, Z. Liu, C. Yan, Y. Yao, N. Chang, H. Zhang, T. Wang, J. Zhang, Monoclinic scheelite bismuth vanadate derived bismuthene nanosheets with rapid kinetics for electrochemically reducing carbon dioxide to formate, Adv. Funct. Mater. 31 (2021), 2006704, https://doi.org/10.1002/adfm.202006704.
[57] G.W. Woyessa, J.-a B. dela Cruz, M. Rameez, C.-H. Hung, Nanocomposite catalyst of graphitic carbon nitride and Cu/Fe mixed metal oxide for electrochemical CO_2 reduction to CO, Appl. Catal. B Environ. 291 (2021), 120052, https://doi.org/10.1016/j.apcatb.2021.120052.
[58] S. Sun, Q. An, M. Watanabe, J. Cheng, H. Ho Kim, T. Akbay, A. Takagaki, T. Ishihara, Highly correlation of CO_2 reduction selectivity and surface electron accumulation: a case study of Au-MoS_2 and Ag-MoS_2 catalyst, Appl. Catal. B Environ. 271 (2020), 118931, https://doi.org/10.1016/j.apcatb.2020.118931.
[59] S.M. Lee, H. Lee, J. Kim, S.H. Ahn, S.T. Chang, All-water-based solution processed Ag nanofilms for highly efficient electrocatalytic reduction of CO_2 to CO, Appl. Catal. B Environ. 259 (2019), 118045, https://doi.org/10.1016/j.apcatb.2019.118045.